JOURNAL OF SPACECRAFT AND ROCKETS
Vol. 30, No. 4, July–August 1993

Enhancements to Viscous-Shock-Layer Technique

Roop N. Gupta*
NASA Langley Research Center, Hampton, Virginia 23681
Kam-Pui Lee†
ViGYAN, Inc., Hampton, Virginia 23666
and
Ernest V. Zoby*
NASA Langley Research Center, Hampton, Virginia 23681

A solution procedure is presented that considerably improves the computational efficiency of the viscous-shock-layer technique, especially for long slender bodies. The "predictor-corrector" procedure suggested for obtaining the shock shape beyond the nose region requires only a single global pass. The accuracy of the present method is demonstrated by comparison with globally iterated results over the entire body and with ground- and flight-test data. The new procedure results in computer run times one-third to one-half of the times required for the full-body global iteration procedure. Furthermore, the algebraic expressions used to specify the initial shock shape eliminate the need for a shock shape generated by external means and permit immediate introduction of the full viscous-shock-layer equations.

Nomenclature

Alt = altitude
C_i = mass fraction of species i, ρ_i/ρ
C_p = frozen specific heat of mixture, $\sum_i C_i C_{p,i}$
$C_{p,i}$ = specific heat of species, $C^*_{p,i}/C^*_{p,\infty}$
D_{ij} = binary diffusion coefficients
H = total enthalpy of mixture, H^*/U^{*2}_∞
h = enthalpy of mixture, $\sum_i C_i h_i$
h_i = enthalpy of species i, h_i^*/U^{*2}_∞
J_i = diffusion mass flux of species i, $(\mu Le/Pr)(\partial C_i/\partial n)$
K = thermal conductivity of mixture, $K^*/\mu^*_{\text{ref}} C^*_{p,\infty}$
k^*_w = surface catalytic recombination rate
Le = Lewis number, $\rho^* D^*_{ij} C^*_p/K^*$
$\bar{M}^*$ = molecular weight of mixture
M_i^* = molecular weight of species i
N_s = number of reacting species
n = coordinate measured normal to the body, n^*/R^*_N
p = pressure, $p^*/\rho^*_\infty U^{*2}_\infty$
Pr = Prandtl number, $\mu^* C^*_p/K^*$
q_w = wall heat transfer rate, $q^*_w/(\rho^*_\infty U^{*3}_\infty)$
R^* = universal gas constant
R^*_N = nose radius
Re_∞ = Reynolds number, $\rho^*_\infty U^*_\infty R^*_N/\mu^*_\infty$
r = radius of the body surface r^*/R^*_N
s = coordinate measured along the body surface, s^*/R^*_N
T = temperature, T^*/T^*_{ref}
t = entry time from 121.9 km (400,000 ft) altitude
U^*_∞ = freestream velocity
u = velocity component tangent to body surface, u^*/U^*_∞
v = velocity component normal to body surface, v^*/U^*_∞
$\dot{w}_i$ = mass rate of formation of species i, $\dot{w}_i^* R^*_N/\rho^*_\infty U^*_\infty$
x/L = nondimensionalized Shuttle axial length
α = shock angle defined in Fig. 1
γ_i = catalytic recombination coefficient
Δh_i^f = heat of formation of species i
ϵ = Reynolds number parameter, $\sqrt{\mu^*_{\text{ref}}/\rho^*_\infty U^*_\infty R^*_N}$
θ = body angle defined in Fig. 1
κ = body curvature, $\kappa^* R^*_N$
μ = viscosity of mixture, μ^*/μ^*_{ref}
μ^*_{ref} = reference viscosity, $\mu^*(T^*_{\text{ref}})$
ρ = density of mixture, ρ^*/ρ^*_∞
ρ^*_{ref} = reference density, 2.621×10^{-4} kg/m^3

Subscripts

c = calculated
e = extrapolated
i = ith species
m = body station
s = shock
w = wall
∞ = freestream

Superscripts

A = atom
M = molecule
$*$ = dimensional quantity

Introduction

THE calculation of hypersonic viscous flowfields over a wide range of Reynolds number is of prime interest to the designer of re-entry aerospace vehicles. Recently, the interest has focused on a diverse group of vehicles such as the National Aero-Space Plane (NASP), Aeroassist Space Transfer Vehicle (ASTV), and Personnel Launch System (PLS).[1-3]

The aerothermodynamic issues concerning the aerospace vehicles can be studied by solution of the boundary-layer, viscous-shock-layer (VSL), parabolized Navier-Stokes (PNS), or full Navier-Stokes equations. For analyzing the hypersonic flow past blunt bodies, the VSL equations represent an intermediate level of approximation and are considered the most efficient[4,5] for analyzing flows past an axisymmetric body at 0-deg angle of attack due to small computational times and

Received June 3, 1992; presented as Paper 92-2897 at the AIAA 27th Thermophysics Conference, Nashville, TN, July 6–8, 1992; revision received Sept. 21, 1992; accepted for publication Sept. 21, 1992.

*Aerospace Engineer, Aerothermodynamics Branch, Space Systems Division. Associate Fellow AIAA.
†Research Engineer. Senior Member AIAA.

computer storage requirements. As a result, the VSL equations are typically employed to investigate various flowfield technology areas requiring a detailed flowfield physics. These technology areas include turbulence models,[4] slip effects,[5] flowfield chemistry,[6,7] and radiatively coupled ablation.[8,9]

The steady-state VSL equations are of mixed hyperbolic-elliptic type in the subsonic nose region of a blunt body and are of mixed hyperbolic-parabolic type in the streamwise direction where the flow becomes supersonic. The streamwise gradients of the pressure and normal velocity cause the VSL equations to be elliptic in the subsonic nose region. To overcome this elliptic nature of the VSL equations, Davis[10] obtained solutions of the full VSL equations for a wide-angle body by relaxing the shock shape obtained from the thin-layer solution. For a slender body (where the approach of Davis[10] results in divergent solutions), Gupta et al.[4] and Lee et al.[5] successively relaxed the shock shape from a wide-angle body to a slender body after coupling[11,12] the normal momentum and global continuity equations. In a further attempt to reduce run time for long slender blunted cones, it was suggested in Ref. 4 that the global iteration process encompass only the region just downstream of the shock recompression zone and that a marching procedure with linear extrapolation of the shock shape be employed over the remainder of the vehicle length. This approach results in a considerable saving of computational time, especially for reacting-gas flow calculations. However, since the shock recompression zone persists over an extensive region for smaller body angles, limiting the global iterations only through the shock recompression zone may still require considerable computational time. The question may then be asked if accuracy can be maintained and computer run time further reduced by limiting global iterations to a region upstream of the shock recompression zone or, preferably, just over the nose region (where the subsonic or elliptic flowfield prevails).

A large number of Russian papers has appeared recently on the solution of VSL equations. These papers (see for example Ref. 13) basically follow the approach of Davis[10] and have obtained solutions by carrying out multiple global iterations along the entire length of the body.

This paper presents a solution procedure in which the global iterations are limited only to the nose region of a blunt body. In addition, unlike the approaches of Refs. 4, 5, 14, and 15, an input shock shape obtained from a different solution is not required in the current approach. Furthermore, the full VSL equations are solved without the need to solve first the thin-layer equations as was done in Refs. 10 and 16. An algebraic expression is used for prescribing the initial shock shape in the nose region. This shape is globally iterated to obtain a converged shock. Beyond the nose region, a predictor-corrector method, based on Taylor's series extrapolation with correction through local iterations, is employed to obtain the converged shock shape at each body station. A similar marching method employing approximate VSL equations was presented recently[17] in the shock-oriented coordinates. The present procedure is for the direct method in the body-oriented coordinate system. This paper also provides the correct shock boundary condition for enthalpy (for real-gas flows) which is in error in earlier papers.[16] Finally, the wall boundary condition for the concentration of oxygen has been modified from an earlier work.[18]

Analysis

The analysis presented here gives a brief discussion of the flow governing equations, the boundary conditions, thermodynamic and transport properties, expressions for the shock shape and shock-layer thickness, and the method of solution.

Conservation Equations

The VSL equations for a perfect gas were obtained in Ref. 10, whereas those for the equilibrium and nonequilibrium multicomponent gas mixtures were developed in Ref. 16. These equations were obtained from the steady-state Navier-Stokes equations by keeping terms up to second-order in the inverse square root of the Reynolds number ϵ. Consequently, one set of equations is solved for both the inviscid and viscous regions of the shock layer. The nondimensional form of the VSL equations in a body-oriented coordinate system (shown in Fig. 1) for a nonequilibrium axisymmetric flow under the assumption of binary diffusion are as follows:

Global Continuity:

$$\frac{\partial}{\partial s}[(r + n\cos\theta)\rho u] + \frac{\partial}{\partial n}[(1 + n\kappa)(r + n\cos\theta)\rho v] = 0 \quad (1)$$

s momentum:

$$\rho\left(\frac{u}{1+n\kappa}\frac{\partial u}{\partial s} + v\frac{\partial u}{\partial n} + \frac{uv\kappa}{1+n\kappa}\right) + \frac{1}{1+n\kappa}\frac{\partial p}{\partial s} = \epsilon^2\left\{\frac{\partial}{\partial n}\left[\mu\left(\frac{\partial u}{\partial n} - \frac{u\kappa}{1+n\kappa}\right)\right] + \mu\left(\frac{2\kappa}{1+n\kappa} + \frac{\cos\theta}{r+n\cos\theta}\right)\left(\frac{\partial u}{\partial n} - \frac{u\kappa}{1+n\kappa}\right)\right\} \quad (2)$$

n momentum:

$$\rho\left(\frac{u}{1+n\kappa}\frac{\partial v}{\partial s} + v\frac{\partial v}{\partial n} - \frac{u^2\kappa}{1+n\kappa}\right) + \frac{\partial p}{\partial n} = 0 \quad (3)$$

Energy (temperature):

$$\rho C_p\left(\frac{u}{1+n\kappa}\frac{\partial T}{\partial s} + v\frac{\partial T}{\partial n}\right) - \left(\frac{u}{1+n\kappa}\frac{\partial p}{\partial s} + v\frac{\partial p}{\partial n}\right) = \epsilon^2\left[\frac{\partial}{\partial n}\left(K\frac{\partial T}{\partial n}\right) + \left(\frac{\kappa}{1+n\kappa} + \frac{\cos\theta}{r+n\cos\theta}\right)\left(K\frac{\partial T}{\partial n}\right) + \frac{\mu Le}{Pr}\left(\sum_{i=1}^{N_s} C_{p,i}\frac{\partial C_i}{\partial n}\right)\frac{\partial T}{\partial n} + \mu\left(\frac{\partial u}{\partial n} - \frac{\kappa u}{1+n\kappa}\right)^2\right] - \sum_{i=1}^{N_s} h_i\dot{w}_i \quad (4)$$

Species continuity:

$$\rho\left(\frac{u}{1+n\kappa}\frac{\partial C_i}{\partial s} + v\frac{\partial C_i}{\partial n}\right) = \dot{w}_i + \frac{\epsilon^2}{(1+n\kappa)(r+n\cos\theta)} \times \left\{\frac{\partial}{\partial n}\left[(1+n\kappa)(r+n\cos\theta)\frac{\mu Le}{Pr}\frac{\partial C_i}{\partial n}\right]\right\} \quad (5)$$

State:

$$p = \rho TR^*/\bar{M}^*C^*_{p,\infty} \quad (6)$$

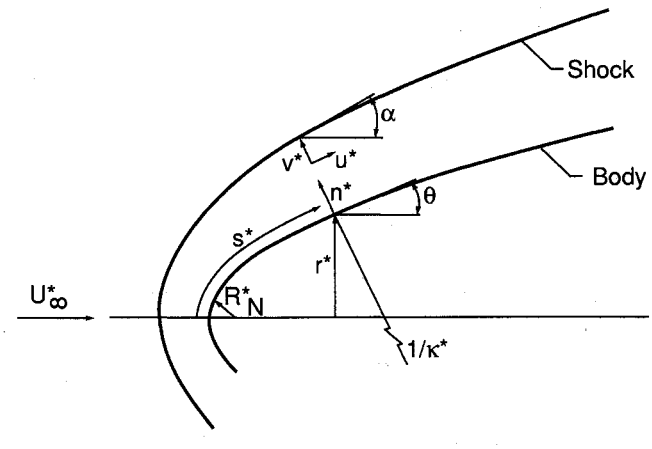

Fig. 1 Coordinate system.

For equilibrium flow, the species continuity equation is not needed and the energy equation is replaced by the following:

Energy:

$$\rho\left(\frac{u}{1+n\kappa}\frac{\partial H}{\partial s}+v\frac{\partial H}{\partial n}\right)-v\frac{\partial p}{\partial n}+\frac{\rho\kappa u^2 v}{1+n\kappa}=\epsilon^2\left[\frac{\partial \Phi}{\partial n}+\Phi\left(\frac{\kappa}{1+n\kappa}+\frac{\cos\theta}{r+n\cos\theta}\right)\right] \tag{7a}$$

where

$$H=h+(u^2/2) \tag{7b}$$

$$\Phi=\frac{\mu}{Pr}\left[\frac{\partial H}{\partial n}+(Le-1)\sum_{i=1}^{N_s}h_i\frac{\partial C_i}{\partial n}+(Pr-1)u\frac{\partial u}{\partial n}-\frac{Pr\kappa u^2}{1+n\kappa}\right] \tag{7c}$$

For perfect-gas flow, again the species continuity equation is not required. For this case, Eqs. (1–3) with Eqs. (6) and (7) are the flow conservation equations with $\bar{M}^*$ replaced by the molecular weight of the perfect gas in Eq. (6) and Φ in Eq. (7a) is defined as

$$\Phi=\frac{\mu}{Pr}\left[\frac{\partial H}{\partial n}+(Pr-1)u\frac{\partial u}{\partial n}-\frac{Pr\kappa u^2}{1+n\kappa}\right] \tag{7d}$$

in place of Eq. (7c).

Gas-Phase Reactions

The number of species chosen in the chemical models for nonequilibrium and equilibrium flows is the same as that used with the existing globally iterative solutions. For nonequilibrium air flow, a five-species (N_2, O_2, N, O, and NO) chemical model is used to evaluate the species production terms $\dot{w}_i$ that appear in the energy and species continuity equations. The expressions and the reaction rates used to evaluate $\dot{w}_i$ in the present study are taken from Ref. 19 and are similar to those of Ref. 20. Details for the evaluation of $\dot{w}_i$ are provided in Ref. 6.

The species concentrations are determined by a free-energy minimization calculation procedure of Ref. 21 for equilibrium air flow. A nine-species (O_2, N_2, O, N, NO, O^+, N^+, NO^+, and e^-) chemical model is used.

Boundary Conditions

The boundary conditions at the shock are calculated by using the Rankine-Hugoniot relations. For perfect-gas calculations, these relations are exact and give the shock values directly. The flow behind the shock, however, is assumed to be either in chemical equilibrium or frozen at the freestream composition for equilibrium and nonequilibrium calculations, respectively. For these calculations, the shock quantities are obtained by an iterative procedure[16] from the Rankine-Hugoniot relations. Equation (38) of Ref. 16 for the shock boundary condition for enthalpy h_s given below

$$h_s=\frac{1}{M_\infty^2(\gamma_\infty-1)}+\frac{\sin^2\alpha}{2}\left(1-\frac{1}{\rho_s^2}\right) \tag{8a}$$

must be modified as

$$h_s=\sum_{i=1}^{N_s}C_{i\infty}\left[\int_{298}^{T^*}C_{p,i}^*\,dT^*\right]\Big/U_\infty^{*2}+\sum_{i=1}^{N_s}C_{i\infty}[(\Delta h_i^{f*})_{T=298\text{ K}}]/U_\infty^{*2}+\frac{\sin^2\alpha}{2}\left(1-\frac{1}{\rho_s^2}\right) \tag{8b}$$

The second term on the right-hand side of Eq. (8b) is zero for air because only N_2 and O_2 are present in the freestream. The computed enthalpy of this investigation as well as that of Ref. 16 is based on a reference temperature of 298 K. The first term on the right-hand side of Eq. (8a), however, implies a reference temperature of 0 K. Using Eq. (8a) in place of Eq. (8b) significantly influences the value of h_s for small values of the shock angle α.

At the wall, the no-slip and no-temperature jump boundary conditions are used. The wall temperature is a specified value. For the equilibrium flow, the wall species concentration is obtained from the free-energy minimization method for the given wall temperature and pressure.

The wall concentrations of O and N for the nonequilibrium flow are governed by the catalytic recombination rate k_{w_i} and are obtained from the net mass flux of O and N at the surface[22]:

$$J_i^A=-(k_{w_i}/\epsilon^2)\rho_i \tag{9a}$$

or

$$\frac{\partial C_i}{\partial n}-\frac{k_{w_i}\rho}{Le\,\mu\epsilon^2}C_i=0 \tag{9b}$$

where k_{w_i} is a recombination rate. The catalytic recombination coefficient γ_i is related to dimensional $k_{w_i}^*$ by

$$\gamma_i=\sqrt{2\pi M_i^*/R^*T^*}\;k_{w_i}^* \tag{10}$$

and is obtained from

$$\gamma_N=0.071\exp(-2219/T_w^*) \tag{11}$$

$$\gamma_O=0.2849(\rho_\infty^*/\rho_{\text{ref}}^*)\exp(-5301.6/T_w^*) \tag{12}$$

where ρ_∞^* is the freestream density.

Equation (11) is obtained from Ref. 23, and Eq. (12) is a modified form of the expression for γ_O given as Eq. (7) in Ref. 18. The reasons for the differences in the present expression for γ_O given here and that of Ref. 18 are the use of better streamwise grid resolution and correction of the reference temperature for h_s [see Eq. (8b)] as well as that of a coding error in the calculation of Prandtl number and thermal conductivity.

The concentrations of O_2 and N_2 are obtained from the net mass flux of these two species at the surface[22]:

$$J_i^M=(k_{w_i}/\epsilon^2)\rho_i \tag{13a}$$

From Eqs. (9a) and (13a), a simpler boundary condition is obtained for O_2 and N_2:

$$\left(\frac{\partial C_i}{\partial n}\right)_M=-\left(\frac{\partial C_i}{\partial n}\right)_A \tag{13b}$$

where A = O for $M = O_2$ and A = N for $M = N_2$. The right-hand side of Eq. (13b) is obtained from Eq. (9b). A boundary condition for NO, consistent with Eqs. (9b) and (13b), is obtained by assuming the surface to be noncatalytic with respect to NO:

$$\frac{\partial C_{NO}}{\partial n}=0 \tag{13c}$$

For noncatalytic and fully catalytic surfaces, the boundary conditions employed, respectively, are

$$\frac{\partial C_i}{\partial n}=0 \tag{14}$$

$$(C_i)_w=(C_i)_\infty \tag{15}$$

Table 1 Constants for shock shapes for $5 \leq \theta \leq 45$ deg

	Constants								
	Perfect gas			Nonequilibrium flow			Equilibrium flow		
Type of body	K_2	K_3	K_4	K_2	K_3	K_4	K_2	K_3	K_4
Sphere cone	3.8	0.2	−0.0625	3.8	0.2	−0.125	4.8	0.2	−0.0625
Hyperboloid	1.4	0.1	−0.0050	1.4	0.1	−0.005	1.4	0.1	−0.0050

The total heat transferred to the wall due to conduction and diffusion for nonequilibrium and equilibrium cases, respectively, is

$$q_w = \epsilon^2\left(K\frac{\partial T}{\partial n} + \frac{\mu Le}{Pr}\sum_{i=1}^{N_s} h_i\frac{\partial C_i}{\partial n}\right)_w \tag{16}$$

$$= \epsilon^2\frac{\mu}{Pr}\left[\frac{\partial H}{\partial n} + (Le-1)\sum_{i=1}^{N_s} h_i\frac{\partial C_i}{\partial n}\right]_w \tag{17}$$

The heat transfer rate for a perfect gas is

$$q_w = \epsilon^2\frac{\mu}{Pr}\frac{\partial H}{\partial n} \tag{18}$$

Thermodynamic and Transport Property

Thermodynamic properties for specific heat, enthalpy, and free energy and transport properties for viscosity and thermal conductivity are required for each species considered. Values for these properties are obtained by using curve fits of Ref. 19.

The mixture viscosity with ionized species (for equilibrium air calculations) is obtained by the method of Armaly and Sutton.[24] For nonequilibrium calculations with five species, the semiempirical method of Wilke[25] is used to calculate the gas-mixture viscosity. Perfect-gas viscosity is obtained from Sutherland's law. The Prandtl number is set equal to 0.72 for all of the calculations, whereas the Lewis number is assigned a value of 1.4 for the equilibrium and nonequilibrium calculations with an assumption of binary diffusion.

Method of Solution

The method of solution for the elliptic nose region is similar to that given in Refs. 4–6 and requires multiple global passes to obtain a converged shock shape (and the solution). Beyond the nose region, however, a single global pass "predictor-corrector" is employed for obtaining the shock shape and a converged solution. A brief description of the solution method for the governing equations is given first in this section before providing details for the shock marching procedure.

Overall Procedure

The second-order partial differential equations for the conservation of streamwise momentum, energy, and species are written in the standard parabolic form[4,6] and their finite difference forms are solved sequentially by a tridiagonal solution procedure. The first-order continuity and normal momentum equations are coupled (based on initial work of Refs. 11, 12, and 14) to overcome the convergence problems when the normal velocity becomes small or changes sign through the shock layer (including at the shock). The finite difference forms of these coupled equations, which also provide a stable solution for bodies with surface discontinuity, are solved, again, by using a tridiagonal solution method.[4,6] As mentioned earlier, the species continuity equation is not needed for equilibrium flow and the species concentrations are obtained by a free-energy minimization calculation procedure.[21]

It should be mentioned here that the elliptic portion of the pressure gradient term (in the Vigneron condition[4]) is evaluated at the shock and is kept constant across the shock layer. The hyperbolic portion of the pressure gradient term, however, is evaluated locally through a backward differencing scheme. The total pressure gradient term (consisting of the hyperbolic and elliptic parts), therefore, does not have a constant value across the shock layer. This allows the introduction of full VSL equations in the first global pass solution itself.

For the nonequilibrium calculations, a check is made for the conservation of elemental mass fractions. In general, one can solve the elemental continuity equation[16] for each of the elements with multicomponent diffusion. In contrast to multicomponent diffusion, no elemental separation is possible with binary diffusion and elemental mass fractions remain fixed through the shock layer. It therefore becomes redundant to solve the elemental continuity equation for constant elemental mass fractions. A check on the conservation of elemental mass fractions in this case, however, can be made by ensuring that their sum obtained from the species mass fractions does not deviate from unity beyond a specified tolerance. The solution of the species continuity equations (along with other flowfield equations) is iterated at a given body location until this criterion is satisfied. For the equilibrium calculations, again no elemental separation will be present in the absence of a foreign gas injection and/or multicomponent diffusion.

Stagnation Streamline

The solution for bodies with a spherically blunted nose begins along the stagnation streamline. Singularity in the VSL equations along this line is removed through an expansion of the flowfield variables around this line. This procedure reduces the governing partial differential equations to ordinary differential equations, which can readily be integrated along the stagnation streamline.[6]

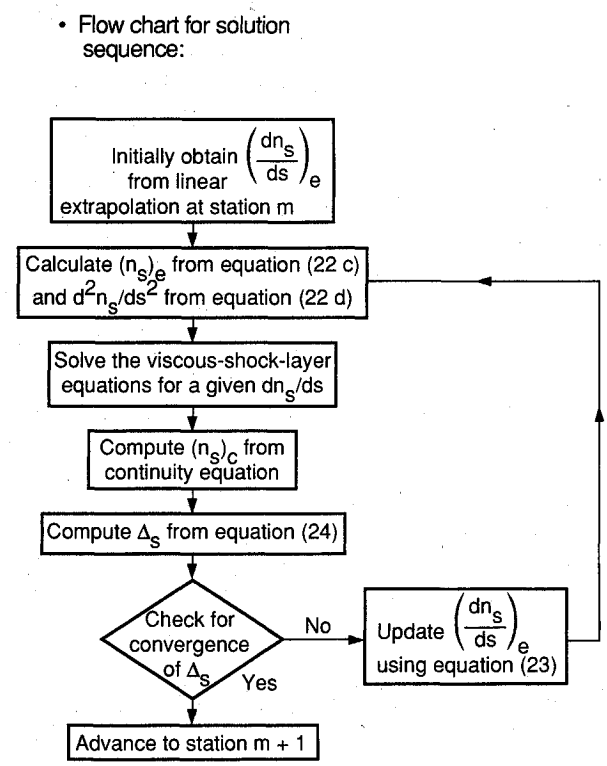

Fig. 2 Flowchart for solution sequence of viscous-shock-layer equations with predictor-corrector method for the shock shape.

Downstream of the Stagnation Streamline

Using the stagnation streamline solution, the VSL equations are solved at the next downstream location by employing a two-point backward difference approximation for the streamwise derivative. The solution is iterated until convergence to a specified criterion. This procedure is repeated at each subsequent body location in the streamwise direction.

Shock Shape and Marching Procedure

The full VSL equations require an initial shock shape as input for the solution method to march in the streamwise direction. The output shock shape from a global pass is used as input for the next pass. This procedure is repeated until the input and output shock shapes for a global pass differ by a value less than a specified value. The initial shock shape can be obtained by various procedures, each requiring considerable computational effort. References 10 and 16, for example, use a thin-layer approximation for the initial global pass. The thin-layer approximation, however, fails for slender bodies with cone angles less than about 30 deg. In the approach of Refs. 4 and 5, a catalog of shock shapes is created by starting from a large body angle (with thin-layer approximation) through sequential reduction in the body angles. One has to store these shock shapes for use in a problem with approximately the same body angle. In Refs. 12–15, the initial shock shape is obtained from an Euler code.

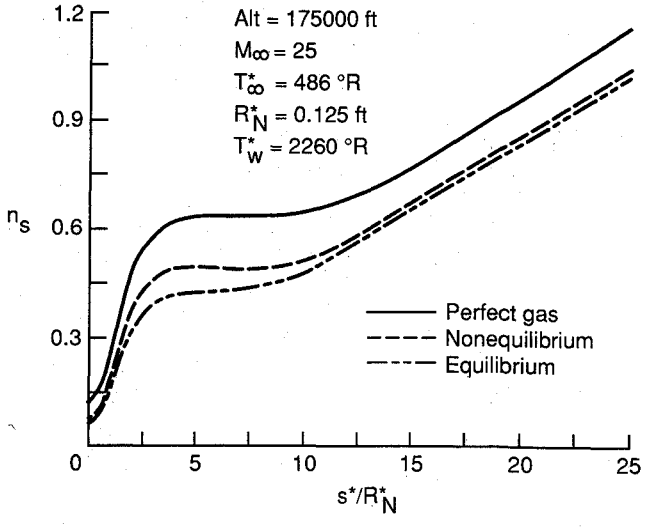

Fig. 3 Shock-standoff-distance for a 20-deg sphere cone with different models for the flowfield chemistry.

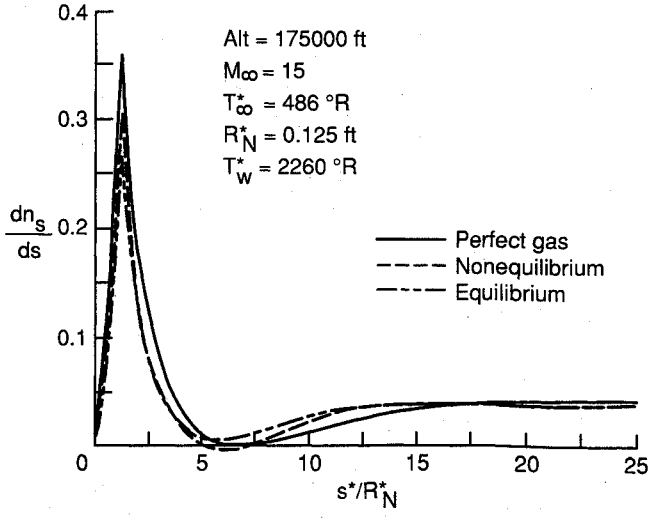

Fig. 4 Shock-standoff-distance gradient for a 20-deg sphere cone with different models for the flowfield chemistry.

In the present approach, a predictor-corrector approach, similar to the method of Ref. 17, is employed for the shock shape. In Refs. 4–7, 10, and 16 the shock angle is obtained from

$$\alpha = \theta + \tan^{-1}\left[\frac{dn_s}{ds}\Big/(1 + n_s\kappa)\right] \tag{19}$$

where dn_s/ds is obtained from a previous global solution (or it is an input quantity) and n_s is the currently computed value. The following shock-angle expressions are developed (from a catalog of shock shapes obtained from the globally iterated solutions) in the present work for predicting an initial shock shape for body angles from 5 to 45 deg (for body angles larger than 45 deg, the assumption $\alpha = \theta$ may be used for the initial global pass since the shock is essentially parallel to the body for large angle bodies):

$$\alpha = \theta + \tan^{-1}[C_1(1 - 0.2/s)(\theta/60)] \tag{20a}$$

where

$$C_1 = C_2\exp[K_1(s - s_{tp})] \tag{20b}$$

$$C_2 = K_2\exp[\sqrt{5/\theta}(1 - \theta/5)] + K_3 \tag{20c}$$

$$K_1 = \begin{cases} 1 & s \le s_{tp} \\ K_4(\theta/5 + 1) & s > s_{tp} \end{cases} \tag{20d}$$

and constants K_2, K_3, and K_4 are provided in Table 1 for different models of flowfield chemistry and body shapes. It should be noted here that the values of C_1 obtained from Eq. (20b) are constrained by the following minimum values:

$$C_1 \ge \begin{cases} 0.06 & \text{for a sphere cone} \\ 0.2/(\theta/5 + 1) & \text{for a hyperboloid} \end{cases} \tag{20e}$$

Furthermore, s_{tp} in Eq. (20d) denotes the sphere-cone tangency-point location. For a hyperboloid, s_{tp} is the same angle sphere-cone tangency-point location. In Eqs. (19) and (20), α and θ are to be used in degree.

The shock angle predicted by Eq. (20) is used in the elliptic subsonic nose dominated region and is corrected through subsequent global passes. [Equation (20) may also be used to specify the shock angle beyond the nose region for the entire body. This equation avoids the need to obtain an initial shock shape from a thin-layer solution.] Downstream of this region, the shock shape is predicted and corrected through a marching scheme requiring no global iterations. The switchover from a globally iterated solution to a "predictor-corrector" scheme for the shock shape is done at a body location:

$$s = 5.0(5/\theta)^{0.4} \tag{21}$$

for the different flowfield chemistry models considered. It should be mentioned here that the streamwise step size (Δs) should be kept about 0.1 through the switchover location and a couple of nose radii beyond for faster convergence of results. Generally, one can use a somewhat larger value of Δs with a globally iterated (over the entire body) solution beyond the location given by Eq. (21). Avoiding global passes for a long body, of course, results in substantial saving of computational time. In the present scheme, the shock angle is obtained from Eq. (19). The value of $(dn_s/ds)_m$ (at the current body location) appearing in this equation is obtained initially ($k = 1$) by assuming and employing the relation

$$\left(\frac{d^2n_s}{ds^2}\right)_m = \left(\frac{d^2n_s}{ds^2}\right)_{m-1} \tag{22a}$$

$$\left(\frac{dn_s}{ds}\right)_m = \left(\frac{dn_s}{ds}\right)_{m-1} + \frac{\Delta s}{2}\left[\left(\frac{d^2n_s}{ds^2}\right)_m + \left(\frac{d^2n_s}{ds^2}\right)_{m-1}\right] \quad (22b)$$

The value of n_s [also required in Eq. (19)] can be extrapolated from the Taylor's series extrapolation

$$(n_{s,m})_e = n_{s,m-1} + \Delta s\left(\frac{dn_s}{ds}\right)_{m-1} + \frac{\Delta s^2}{6}\left[2\left(\frac{d^2n_s}{ds^2}\right)_{m-1} + \left(\frac{d^2n_s}{ds^2}\right)_m\right] \quad (22c)$$

where $(d^2n_s/ds^2)_m$ is computed from

$$\left(\frac{d^2n_s}{ds^2}\right)_m = \frac{2}{\Delta s}\left[\left(\frac{dn_s}{ds}\right)_m - \left(\frac{dn_s}{ds}\right)_{m-1}\right] - \left(\frac{d^2n_s}{ds^2}\right)_{m-1} \quad (22d)$$

In Eqs. (22c) and (22d), subscript m denotes the current body location and e denotes extrapolation.

The earlier extrapolated value of dn_s/ds is now corrected by using the expression

$$\left(\frac{dn_s}{ds}\right)^{k+1} = \left(\frac{dn_s}{ds}\right)^k - \left(\frac{\Delta_s^k}{\Delta_s^k - \Delta_s^{k-1}}\right)\left[\left(\frac{dn_s}{ds}\right)^k - \left(\frac{dn_s}{ds}\right)^{k-1}\right] \quad (23)$$

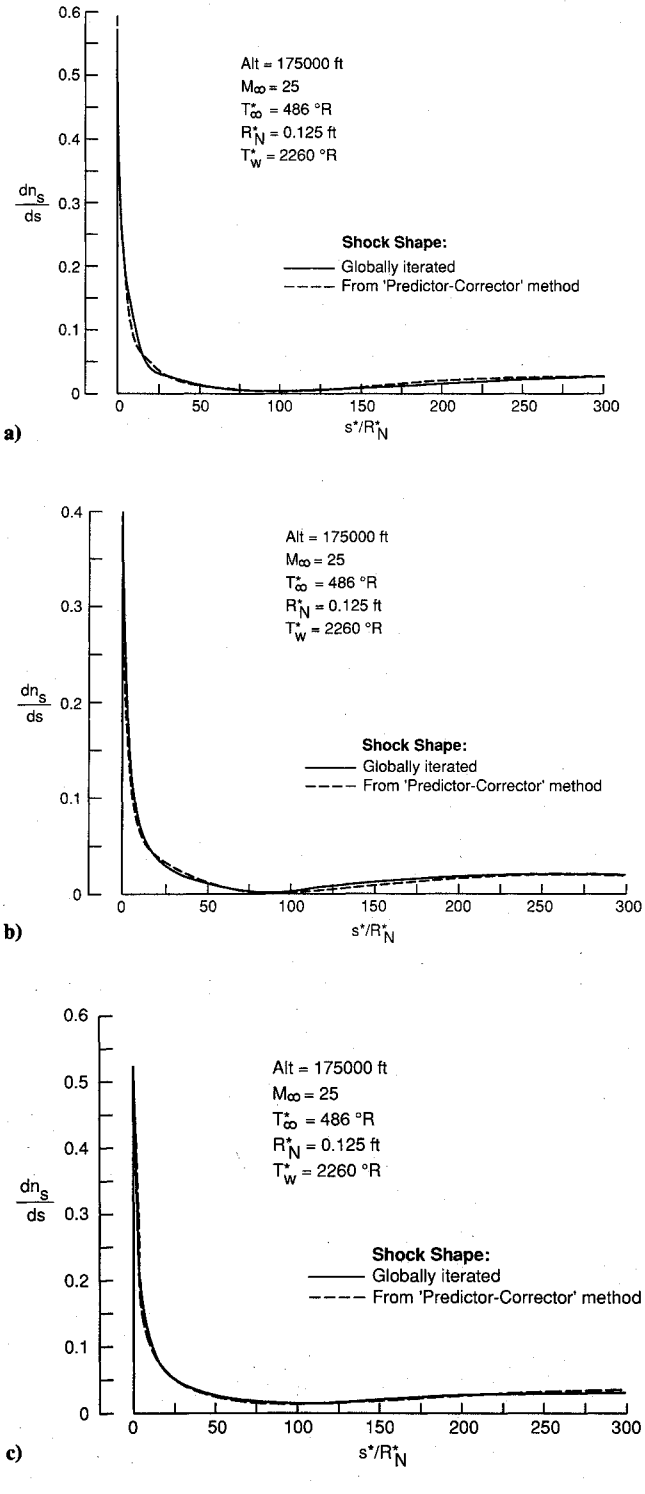

Fig. 5 Shock-standoff-distance gradient for a 5-deg sphere cone: a) perfect gas; b) equilibrium flow; and c) nonequilibrium flow.

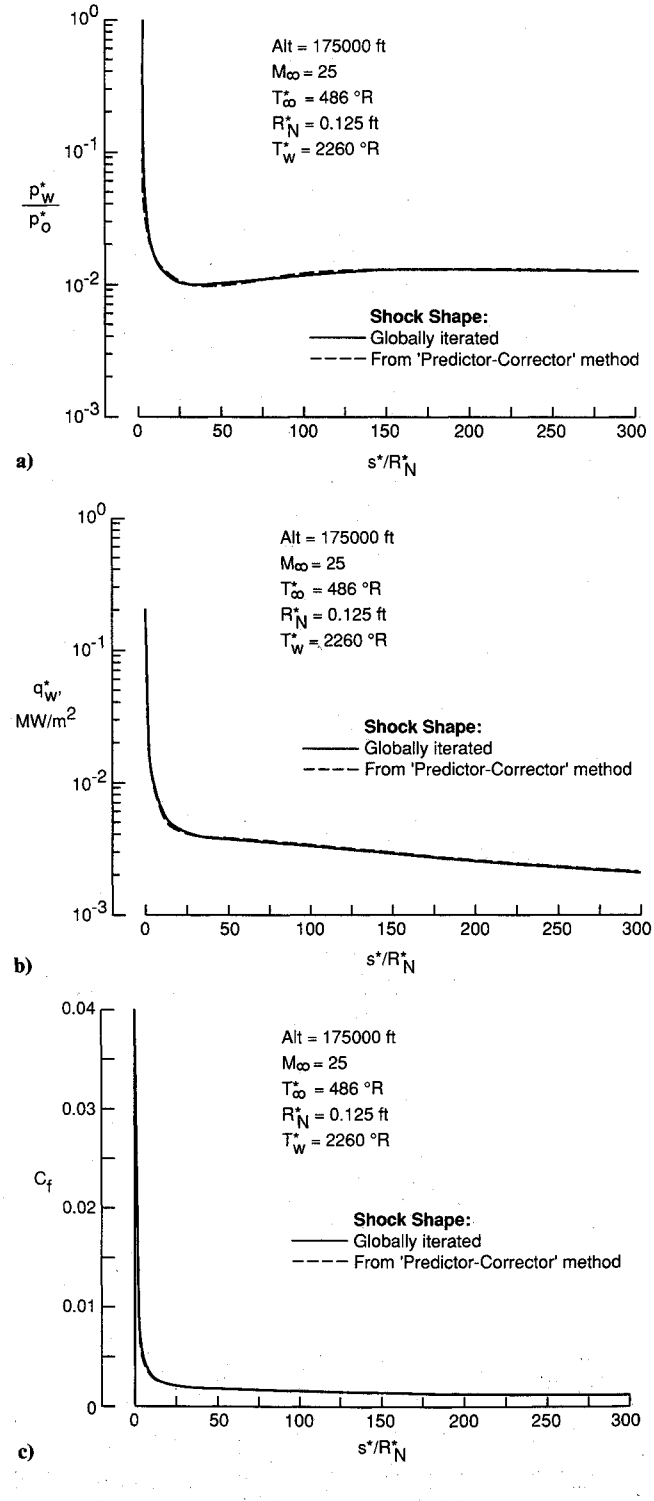

Fig. 6 Distribution of surface quantities for a 5-deg sphere cone (nonequilibrium flow): a) pressure; b) heat transfer rate; and c) skin-friction coefficient.

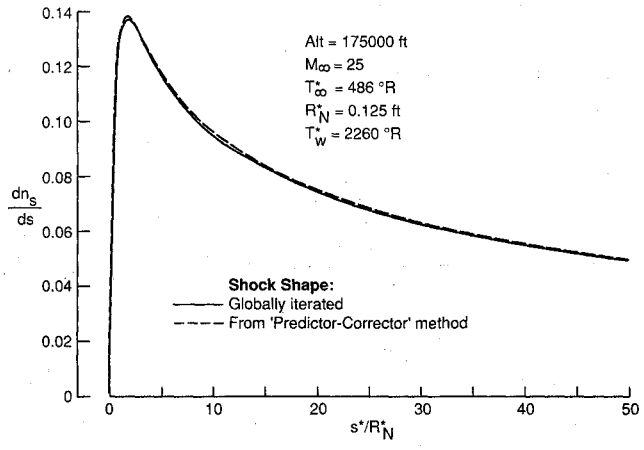

Fig. 7 Shock-standoff-distance gradient for a 5-deg hyperboloid (perfect gas).

where k is a local iteration counter and Δ_s is defined as

$$\Delta_s = \frac{n_{s,c} - n_{s,e}}{n_{s,e}} \tag{24}$$

In this equation, $n_{s,e}$ is obtained from Eq. (22c) and $n_{s,c}$ is calculated from the global continuity, Eq. (1). The solution is iterated at a given body station until Δ_s converges to a specified tolerance. The solution now advances to the next body location. Figure 2 gives a flowchart for solving the VSL equations with this predictor-corrector method for the shock at a given body location. In summary, the shock shape is computed as part of the solution beyond the nose region. In the nose region, shock shape is specified from an algebraic relation and corrected through global passes through that region. Thus, shock shape is not required as an input by the user; it is obtained from the algebraic expression for all of the cases.

Results and Discussion

The present marching scheme with the shock obtained from a predictor-corrector approach has been used to analyze perfect-gas, nonequilibrium, and equilibrium flow over hyperboloids and sphere-cone bodies. The accuracy of these results is demonstrated by comparisons with the earlier scheme requiring an input shock shape and global iterations over the entire body. Comparisons include results for different flowfield chemistry models, body shapes, and body angles. The predicted results are also compared with existing ground- and flight-test data. Finally, a comparison of the computational times required with the two schemes is provided.

For the present calculations, a grid-independent solution was established at an altitude of 175,000 ft for $R_N^* = 0.125$ ft and $M_\infty = 15$. For other calculations, the grid size was varied by employing the relation[22]

$$\Delta n = [(\Delta n)_{\text{Alt}\,=\,175{,}000\text{ ft}}] \frac{[\mu^*_{\text{ref}}/(\rho^*_\infty U^*_\infty R^*_N)]}{[\mu^*_{\text{ref}}/(\rho^*_\infty U^*_\infty R^*_N)]_{\text{Alt}\,=\,175{,}000\text{ ft}}} \tag{25}$$

Flowfield Chemistry

For flows past slender bodies with blunted noses such as a sphere cone, the shock draws closer to the body[26] in the region of overexpansion and recompression (see Fig. 3). This shock behavior is a function of the flow Mach number, nose radius, freestream density, cone half-angle, and the flowfield chemistry. Figure 4 shows that for the flow conditions considered, the shock-standoff-distance gradient is negative for $5 \le s \le 7$ with nonequilibrium flowfield chemistry and is zero at about $s = 6$ for perfect gas. This feature (where $dn_s/ds \le 0$) violates the basic stability condition $dn_s/ds > 0$ of the shock-fitting noniterative PNS codes.[27-30] One may, therefore, not be able to "correctly" compute such flows with the help of these codes without adding excessive amounts of artificial dissipation. This added dissipation, in turn, would compromise the values of various flowfield quantities.[31]

Shock-Standoff-Distance Gradient

Since shock angle is most sensitive to the gradient of shock standoff distance [see Eq. (19)], its predicted values are compared in Fig. 5. Values obtained from the globally iterated method of Ref. 4 and the present method (which computes the shock shape from a predictor-corrector approach) are shown in Figs. 5a–5c for perfect-gas, equilibrium, and nonequilibrium flow, respectively. The two methods give almost the same results through a distance of 300 nose radii. Since globally iterated results have been demonstrated[4,5] to be quite accurate, results obtained by the present method are also considered equally good.

Surface Quantities

A comparison of pressure, heat transfer, and skin-friction coefficient distributions predicted by the two methods is given in Figs. 6a–6c, respectively. For brevity, results are included only for the nonequilibrium flow. Equally good comparison is also obtained for perfect-gas and equilibrium flows.

Body Shapes

The shock-standoff-distance gradient for a 5-deg sphere cone is shown in Fig. 5a, and for a 5-deg hyperboloid in Fig. 7. These results are for a perfect gas. The results obtained from the present predictor-corrector method are in excellent agreement with those obtained from the globally iterated technique for both body shapes of sphere cone and hyperboloid. For the hyperboloid (Fig. 7), results are given only through a

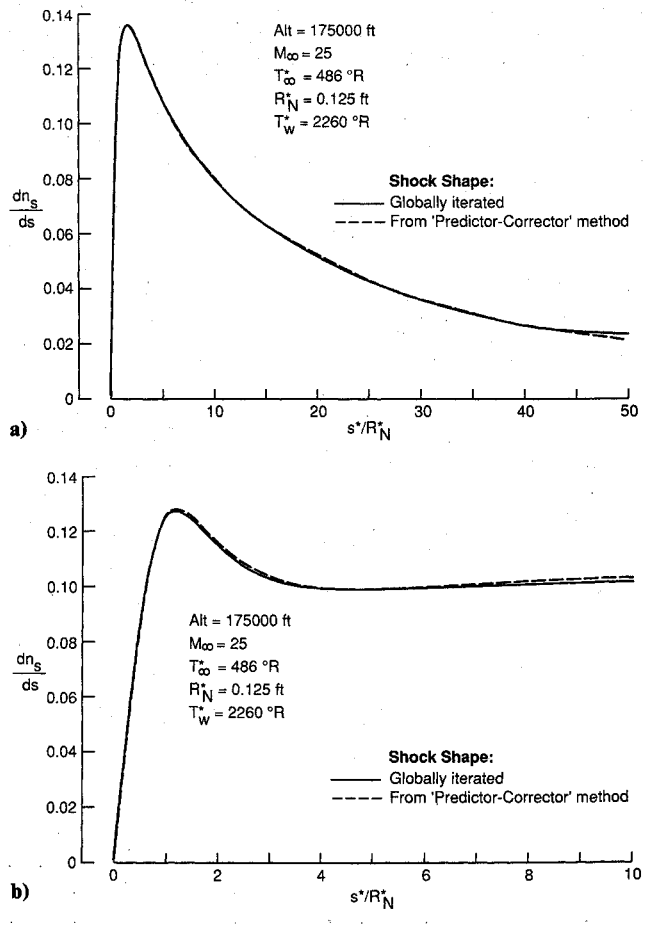

Fig. 8 Shock-standoff-distance gradient for perfect gas: a) 10-deg hyperboloid and b) 45-deg hyperboloid.

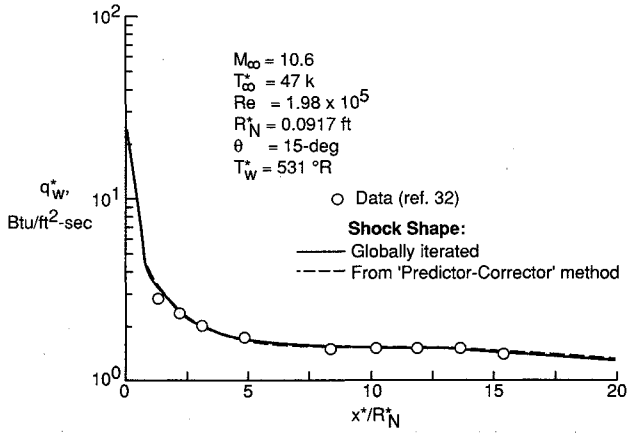

Fig. 9 Comparison of experimental heat transfer rates with predicted results for a 15-deg sphere cone (perfect-gas flow).

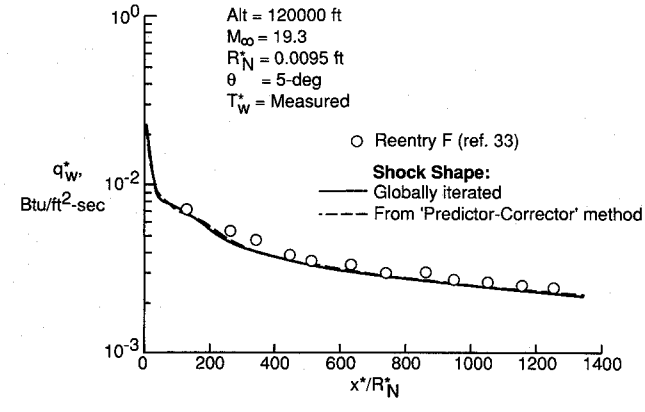

Fig. 10 Comparison of reentry F heating data with predicted results for 5-deg sphere cone (equilibrium air).

distance of 50 nose radii along the body. In this case, unlike the sphere-cone shape bodies, there is no shock recompression zone and no new feature of the flowfield is revealed by carrying out the integration through 300 nose radii. The results presented in Fig. 7 are for a perfect gas; however, similar agreement is seen for equilibrium and nonequilibrium flow calculations.

Body Angles

Figures 8a and 8b show comparison of the shock-standoff-distance gradient for 10- and 45-deg hyperboloids. Results for the two widely different body angles are predicted with a good degree of accuracy with the present method when compared with the globally iterated results. Similar accuracy in the results predicted from the predictor-corrector method is seen for equilibrium and nonequilibrium chemistry conditions.

Experimental Data

In this section, results obtained by using the present predictor-corrector method for the shock shape and the globally iterated technique are compared with ground- and flight-test data. The data consist of surface heating measurements over slender cones and a wide-angle hyperboloid for perfect-gas, equilibrium, and nonequilibrium flowfield chemistry conditions.

Perfect-Gas Comparison

The present method predicts surface heating for a 15-deg sphere cone with a similar degree of accuracy as predicted from the globally iterated method as shown in Fig. 9. Both of the predictions compare quite well (within 10%) with Cleary's experimental data.[32]

Equilibrium-Flow Comparison

Figure 10 gives a comparison of the predicted heating results with the reentry F data of Ref. 33. The predictions for the present method (as well as the globally iterated technique) are within 15% of the flight data for the entire body length.

Nonequilibrium-Flow Comparison

Figure 11 provides a comparison of the heating-rate results obtained by the present and globally iterated methods with those measured[34] along the Shuttle windward centerline for flight STS-2. The predictions have been made by using an equivalent axisymmetric body approach[35] and are for a finite-wall catalycity with the new oxygen recombination-rate expression [Eq. (12)]. Clearly, an excellent agreement is obtained for the present (as well as globally iterated) method with the flight data.

Computer Run Times

The computer run time requirements (measured in CPU seconds) for a 5-deg sphere cone with different models of flowfield chemistry are given in Table 2. To obtain an exact comparison of computational times, the globally iterated results were obtained using an algebraic expression for the initial shock shape for the entire body length. The present method also used the same expression for the nose region. However, there is only a single global pass required for the present predictor-corrector technique (employed for shock shape) beyond the nose region. For the same number of grid points in the normal as well as streamwise direction and same degree of accuracy, the total CPU requirements for the present method are about 32, 39, and 53% of the time required for the globally iterated solution for perfect-gas, nonequilibrium, and equilibrium flows, respectively.

The saving in the run times with the present method is considerably more when compared with the globally iterated method of Refs. 4 and 6. In these references, the shock shape for a slender cone was obtained from the shock shape for a wide-angle cone by sequentially reducing the cone angle in steps of 5-10 deg. For each intermediate cone angle, the global solution was iterated about two times. Thus, considerable computational time was spent (about three times more as compared with the time for the globally iterated solutions given in Table 2) in obtaining solutions for a slender body. The present method, therefore, is very efficient, especially for computing flowfields along long slender bodies.

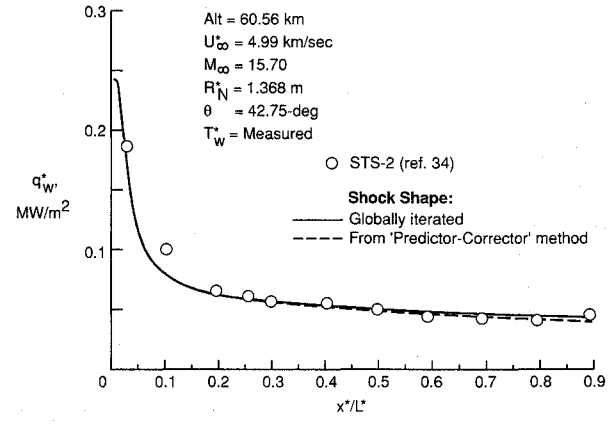

Fig. 11 Comparison of STS-2 heating data wtih predicted results for an equivalent 42.75-deg hyperboloid at 0-deg angle of attack (nonequilibrium air with finite catalytic wall).

Table 2 Run times for 5-deg sphere cone ($R_N^* = 0.125$ ft, $T_w^* = 2260°$R, Alt = 175,000 ft, and $M_\infty = 25$)

	Perfect gas		Nonequilibrium flow		Equilibrium flow	
	Globally iterated shock	Shock from predictor-corrector method	Globally iterated shock	Shock from predictor-corrector method	Globally iterated shock	Shock from predictor-corrector method
Number of body stations	852	852	852	852	852	852
Number of grid points per body station	101	101	101	101	101	101
Number of global passes	5	1[a]	4	1[b]	5	1[a]
Total CPU time, s	455	147	1985	767	15,976	8409
CPU time/body station, s	0.1067	0.1386	0.5824	0.7546	3.7930	6.4720

[a]Solutions over the nose were globally iterated four times.
[b]Solutions over the nose were globally iterated three times.

Concluding Remarks

Contributions have been made to improve computational efficiency of the VSL technique. A procedure is demonstrated that requires global iterations over the nose (subsonic) region from an initial algebraic shock shape. However, beyond the nose region, a predictor-corrector procedure for obtaining the shock shape requires only a single global pass. This approach results in considerable savings (one-third to one-half) in the computational times, especially for long slender bodies, when compared with the generally employed approach of multiple global passes over the entire body length.

The algebraic expressions suggested for the nose region have also been used for obtaining an initial shock shape for the entire length of the body for the globally iterated solutions. The suggested algebraic expressions for the initial shock shape allow solution of the full shock-layer equations even during the first global pass both over the nose region and entire length of the body.

Two corrections have been made to the previously developed VSL method. First, the shock boundary condition for enthalpy for real-gas flows is determined correctly and is in error in earlier papers. Second, the wall boundary condition for the concentration of oxygen has been modified from earlier work.

The accuracy of the presently suggested solution procedure as well as that of the globally iterated method (with initial shock shape prescribed by the suggested algebraic expressions) is demonstrated by comparison with the ground- and flight-test data. A good comparison is obtained between the predicted results and data for different flowfield chemistry models, body shapes, and body angles. The present VSL method provides to the aerothermal designer not only an extremely useful and efficient tool for future technology studies but also a detailed flowfield method with good accuracy.

References

[1]Williams, R. M., "National Aerospace Plane: Technology for America's Future," *Aerospace America,* Vol. 24, No. 11, 1986, pp. 18–22.

[2]Martin, J. A., "Special Section—Orbit-on-Demand Vehicle," *Aerospace America,* Vol. 23, No. 2, 1985, pp. 46–48.

[3]Piland, W. M., Talay, T. A., and Stone, H. W., "The Personnel Launch System," *Aerospace America,* Vol. 28, No. 11, 1990, pp. 18–21 and p. 29.

[4]Gupta, R. N., Lee, K. P., Zoby, E. V., Moss, J. N., and Thompson, R. A., "Hypersonic Viscous Shock-Layer Solutions Over Long Slender Bodies—Part I: High Reynolds Number Flows," *Journal of Spacecraft and Rockets,* Vol. 27, No. 2, 1990, pp. 175–184.

[5]Lee, K. P., Gupta, R. N., Zoby, E. V., and Moss, J. N., "Hypersonic Viscous Shock-Layer Solutions over Long Slender Bodies—Part II: Low Reynolds Number Flows," *Journal of Spacecraft and Rockets,* Vol. 27, No. 2, 1990, pp. 185–193.

[6]Lee, K. P., and Gupta, R. N., "Viscous-Shock-Layer Analysis of Hypersonic Flows over Long Slender Vehicles," NASA CR-189614, March 1992.

[7]Zoby, E. V., Lee, K. P., Gupta, R. N., Thompson, R. A., and Simmonds, A. L., "Viscous Shock-Layer Solutions with Nonequilibrium Chemistry for Hypersonic Flows past Slender Bodies," *Journal of Spacecraft and Rockets,* Vol. 26, No. 4, 1989, pp. 221–228.

[8]Gupta, R. N., Lee, K. P., Moss, J. N., and Sutton, K., "Viscous-Shock-Layer Solutions with Coupled Radiation and Ablation Injection for Earth Entry," AIAA Paper 90-1697, June 1990.

[9]Gupta, R. N., Lee, K. P., Moss, J. N., and Sutton, K., "A Viscous Shock-Layer Analysis of the Martian Aerothermal Environment," AIAA Paper 91-1345, June 1991.

[10]Davis, R. T., "Numerical Solution of the Hypersonic Viscous-Shock-Layer Equations," *AIAA Journal,* Vol. 8, No. 5, 1970, pp. 843–851.

[11]Werle, M. J., Srivastava, B. N., and Davis, R. T., "Numerical Solutions to the Full Viscous Shock Layer Equations Using an ADI Technique," Dept. of Aerospace Engineering, Univ. of Cincinnati, Rept. AFL-74-7-13, Cincinnati, OH, Aug. 1974.

[12]Waskiewicz, J. D., and Lewis, C. H., "Recent Developments in Viscous Shock-Layer Theory," Virginia Polytechnic Inst. and State Univ., VPI and SU Aero. Rept. 079, Blacksburg, VA, March 1978.

[13]Vasil'Yevskii, S. A., Tirskii, G. A., and Utyuzhnikov, S. V., "A Numerical Method for Solving the Equations of a Viscous Shock Layer," *U.S.S.R Comput. Maths. Math. Phys.,* Vol. 27, No. 3, 1987, pp. 64–71 (in English, Pergamon, 1988).

[14]Murray, A. L., and Lewis, C. H., "Hypersonic Three-Dimensional Viscous Shock Layer Flows over Blunt Bodies," *AIAA Journal,* Vol. 16, No. 12, pp. 1279–1286.

[15]Thompson, R. A., Zoby, E. V., Wurster, K. E., and Gnoffo, P. A., "An Aerothermodynamic Study of Slender Conical Vehicles," AIAA Paper 87-1475, June 1987.

[16]Moss, J. N., "Reacting Viscous-Shock-Layer Solutions with Multicomponent Diffusion and Mass Injection," NASA TR R-411, June 1974.

[17]Cheatwood, F. M., and DeJarnette, F. R., "An Approximate Viscous Shock Layer Approach to Calculating Hypersonic Flows About Blunt-Nosed Bodies," AIAA Paper 91-1348, June 1991.

[18] Zoby, E. V., Gupta, R. N., and Simmonds, A. L., "Temperature Dependent Reaction Rate Expressions for Oxygen," *Thermal Design of Aeroassisted Orbital Transfer Vehicles,* edited by H. F. Nelson, Vol. 96, Progress in Astronautics and Aeronautics, AIAA, New York, 1985, pp. 445–464.

[19]Gupta, R. N., Yos, J. M., Thompson, R. A., and Lee, K. P., "A Review of Reaction Rates and Thermodynamic and Transport Properties for an 11-Species Air Model for Chemical and Thermal Nonequilibrium Calculations to 30000K," NASA RP-1232, Aug. 1990.

[20]Blottner, F. G., "Viscous Shock Layer at the Stagnation Point With Nonequilibrium Air Chemistry," *AIAA Journal,* Vol. 7, No. 12, 1969, pp. 2281–2288.

[21]Stroud, C. W., and Brinkley, K. L., "Chemical Equilibrium of Ablation Materials Including Condensed Species," NASA TN D-5391, Aug. 1969.

[22]Gupta, R. N., and Simmonds, A. L., "Stagnation Flowfield Analysis for an Aeroassist Flight Experiment Vehicle," AIAA Paper 88-2613, June 1988.

[23]Scott, C. D., "Catalytic Recombination of Oxygen and Nitrogen in High Temperature Reusable Surface Insulation," *Aerothermodynamics and Planetary Entry,* edited by A. L. Crosbie, Vol. 77, Progress in Astronautics and Aeronautics, AIAA, New York, 1981, pp. 192-212.

[24]Armaly, B. F., and Sutton, K., "Viscosity of Multicomponent Partially Ionized Gas Mixtures," AIAA Paper 80-1495, July 1980.

[25]Wilke, C. R., "A Viscosity Equation for Gas Mixtures," *Journal of Chemical Physics,* Vol 18, No. 4, 1950, pp. 517-519.

[26]Rakich, J. V., and Cleary, J. W., "Theoretical and Experimental Study of Supersonic Steady Flow Around Inclinded Bodies of Revolution," *AIAA Journal,* Vol. 8, No. 3, 1970, pp. 511-518.

[27]Vigneron, Y. C., Rakich, J. V., and Tannehill, J. C., "Calculation of Supersonic Viscous Flow over Delta Wings with Sharp Subsonic Leading Edges," AIAA Paper 78-1137, July 1978.

[28]Shanks, S. P., Srinivasan, G. R., and Nicolet, W. E., "AFWAL Parabolized Navier-Stokes Code: Formulation and User's Manual," Air Force Wright Aeronautical Lab., Wright-Patterson AFB, AFWAL-TR-82-3034, Dayton, OH, June 1982.

[29]Stalnaker, J. F., Nicholson, L. A., Hanline, D. S., and McGraw, E. H., "Improvements to the AFWAL Parabolized Navier-Stokes Code Formulation," Air Force Wright Aeronautical Lab, Wright-Patterson AFB, AFWAL-TR-86-3076, Dayton, OH, Sept. 1986.

[30]Walker, M. A., "SPRINTRUN: A User Friendly Input Processor for the SPRINT Code," Sandia National Labs., Rept. SAND 89-0625, Albuquerque, NM, March 1990.

[31]Macaraeg, M. G., Street, C. L., and Hussaini, M. Y., "Analysis of Artificial Viscosity Effects on Reacting Flows Using a Spectral Multidomain Technique," *Journal of Thermophysics and Heat Transfer,* Vol. 3, No. 1, 1989, pp. 13-18.

[32]Cleary, J. W., "Effects of Angle of Attack and Bluntness on Laminar Heating-Rate Distributions of a 15-Deg Cone at a Mach Number of 10.6," NASA TN-D5450, Oct. 1969.

[33]Howard, F. G., "Thermal Analysis Methods and Basic Heat Transfer Data for a Turbulent Heating Flight Experiment at Mach 20 (Reentry F)," NASA TMX 2282, May 1971.

[34]Hartung, L. C., and Throckmorton, D. A., "Space Shuttle Entry Heating Data Book: Volume I-STS-2," NASA RP-1191, Parts 1 & 2, May 1988.

[35]Zoby, E. V., "Approximate Heating Analysis for the Windward Symmetry Plane of Shuttle-Like Bodies at Large Angle of Attack," *Thermophysics of Atmospheric Entry,* edited by T. E. Horton, Vol. 82, Progress in Astronautics and Aeronautics, AIAA, New York, 1982, pp. 229-247.